Geophysical Journal International

Geophys. J. Int. (2014) **196,** 712–723
Advance Access publication 2013 November 21

doi: 10.1093/gji/ggt425

A spherical shell numerical dynamo benchmark with pseudo-vacuum magnetic boundary conditions

A. Jackson,[1] A. Sheyko,[1] P. Marti,[1,*] A. Tilgner,[2] D. Cébron,[1] S. Vantieghem,[1] R. Simitev,[3,4,5] F. Busse,[4,6] X. Zhan,[4] G. Schubert,[4] S. Takehiro,[7] Y. Sasaki,[8] Y.-Y. Hayashi,[9] A. Ribeiro,[4] C. Nore[10,11] and J.-L. Guermond[12]

[1] *Institute of Geophysics, ETH Zurich, Zurich* 8092, *Switzerland. E-mail: ajackson@ethz.ch*
[2] *Institute of Geophysics, University of Göttingen, D-*37077 *Göttingen, Germany*
[3] *Solar Physics, Hansen Experimental Physics Laboratory, Stanford University, CA* 94305, *USA*
[4] *Department of Earth and Space Sciences, University of California, Los Angeles, CA* 90095, *USA*
[5] *School of Mathematics and Statistics, University of Glasgow, Glasgow, G*12 *8QW, UK*
[6] *Institute of Physics, University of Bayreuth, D-*95440 *Bayreuth, Germany*
[7] *Research Institute for Mathematical Sciences, Kyoto University, Kyoto, Japan*
[8] *Department of Mathematics, Kyoto University, Kyoto, Japan*
[9] *Center for Planetary Science/Department of Earth and Planetary Sciences, Kobe University, Kobe, Japan*
[10] *Laboratoire d'Informatique pour la Mécanique et les Sciences de l'Ingénieur, CNRS UPR* 3251, *BP* 133, *F-*91403 *Orsay cedex, and Université Paris-Sud* 11, *Paris, France*
[11] *Institut Universitaire de France,* 103, *bd Saint-Michel, F-*75005 *Paris, France*
[12] *Department of Mathematics, Texas A&M University* 3368 *TAMU, College Station, TX* 77843-3368, *USA*

Accepted 2013 October 10. Received 2013 October 9; in original form 2013 May 9

SUMMARY

It is frequently considered that many planetary magnetic fields originate as a result of convection within planetary cores. Buoyancy forces responsible for driving the convection generate a fluid flow that is able to induce magnetic fields; numerous sophisticated computer codes are able to simulate the dynamic behaviour of such systems. This paper reports the results of a community activity aimed at comparing numerical results of several different types of computer codes that are capable of solving the equations of momentum transfer, magnetic field generation and heat transfer in the setting of a spherical shell, namely a sphere containing an inner core. The electrically conducting fluid is incompressible and rapidly rotating and the forcing of the flow is thermal convection under the Boussinesq approximation. We follow the original specifications and results reported in Harder & Hansen to construct a specific benchmark in which the boundaries of the fluid are taken to be impenetrable, non-slip and isothermal, with the added boundary condition for the magnetic field **B** that the field must be entirely radial there; this type of boundary condition for **B** is frequently referred to as 'pseudo-vacuum'. This latter condition should be compared with the more frequently used insulating boundary condition. This benchmark is so-defined in order that computer codes based on local methods, such as finite element, finite volume or finite differences, can handle the boundary condition with ease. The defined benchmark, governed by specific choices of the Roberts, magnetic Rossby, Rayleigh and Ekman numbers, possesses a simple solution that is steady in an azimuthally drifting frame of reference, thus allowing easy comparison among results. Results from a variety of types of code are reported, including codes that are fully spectral (based on spherical harmonic expansions in angular coordinates and polynomial expansions in radius), mixed spectral and finite difference, finite volume, finite element and also a mixed Fourier-finite element code. There is good agreement among codes.

Key words: Non-linear differential equations; Electromagnetic theory; Dynamo: theories and simulations.

[*] Now at: Department of Applied Mathematics, University of Colorado, Boulder, CO 80309, USA.

1 INTRODUCTION

Many planets possess magnetic fields that are thought to be generated by thermal and compositional convection within their electrically conducting cores, creating the so-called self-excited dynamo mechanism. Since the appearance of the first 3-D self-consistent Boussinesq models of thermal convection almost 20 yr ago (Glatzmaier & Roberts 1995; Kageyama *et al.* 1995), interest has grown in calculating numerical solutions to this physical system. The underlying equations that must be solved are those of momentum conservation, magnetic field generation and heat transfer. Considering the non-trivial nature and non-linearity of these underlying equations, there remains a need to verify that the computer codes provide accurate solutions to the physical system; it is also important to provide simple reference solutions that allow newly developed codes to check that they are correct implementations of the physics, and to allow these codes to assess their accuracy. The provision of a relatively simple solution with clear diagnostics we term as a *benchmark*, and this particular benchmark grew out of discussions initiated at the Studies of the Earth's Deep Interior meeting held in Leeds in 2012.

In geophysics, benchmark solutions were provided for mantle convection in cartesian geometries some decades ago, and in geomagnetism a very useful benchmarking exercise was coordinated by U. Christensen subsequent to the discovery of a particularly simple dynamo solution (Christensen *et al.* 2001; Christensen *et al.* 2009, hereinafter B1). This benchmark exercise was set in the geometry of a spherical shell, with convection driven by a temperature difference between an inner core and the outer boundary of the spherical shell. In the present work we remain with this geometry, it being the appropriate geometry for the core of the Earth. In B1 three different benchmarks were devised, of both a hydrodynamic and magnetohydrodynamic nature, these latter benchmarks being convectively driven dynamos (supporting magnetic fields). It is the purpose of this work to study a modification of B1 first presented by Harder & Hansen (2005). The modification of the magnetic boundary condition from that of B1 is designed to allow computer codes that are not based on spherical harmonics in the angular direction to conveniently compute solutions. This is an important development in view of the fact that many new solution strategies are being developed that are based on 'local methods', examples of which can be found in Section 4. Central to these benchmarks is the fact that all of them possess simple solutions, in the form of steadily azimuthally drifting convection and magnetic fields. Consequently, kinetic and magnetic energies remain constant and, together with other properties, these provide very clear diagnostics that are amenable to reproduction by different numerical techniques.

The modification of the magnetic boundary conditions that we implement requires that the magnetic field be purely radial on the boundary. Since this condition is approximated by the physical conditions arising from a boundary made from very high permeability material (sometimes termed 'ferromagnetic material'), the boundary conditions are sometimes referred to as 'ferromagnetic boundary conditions' or 'pseudo-vacuum conditions'. In a spherical shell the effect of these types of boundary conditions on dynamo action has been studied by Guervilly & Cardin (2010) and Roberts *et al.* (2010). They have been used for almost 20 yr since the pioneering paper of Kageyama *et al.* (1995).

Our benchmarking exercise has attracted submissions from authors implementing a wide assortment of computer codes. Of the eight different results submitted, four are computed using a spectral method (involving spherical harmonics in the angular directions) and three are computed with so-called local methods, namely finite volume or finite element methods; there is also one mixed 'global-local' method. A discussion of the performance of such codes on the original B1 can be found in Wicht *et al.* (2009). Of interest is the fact that the local methods use different approaches to ensuring that magnetic fields are divergence-free. It is well known that writing the magnetic field $\mathbf{B}$ in terms of a vector potential $\mathbf{A}$ as $\mathbf{B} = \nabla \wedge \mathbf{A}$ will automatically satisfy the required solenoidality condition. But another approach is to introduce a fictitious 'magnetic pressure' (Brackbill & Barnes 1980; Tóth 2000), essentially a Lagrange multiplier for the imposition of the zero divergence constraint. Of the groups taking part, three use the latter approach while one uses the $\mathbf{A}$ formulation.

The present benchmarking exercise has a sister exercise that is set in a full sphere geometry, described in Marti *et al.* (2013); this full sphere geometry is potentially challenging for some codes as a result of the presence of a coordinate singularity at $r = 0$ when one treats the governing equations in the sphere in spherical coordinates (r, θ, ϕ) that are presumably convenient from the point of view of boundary conditions. Flows in the first two benchmarks of Marti *et al.* (2013) are driven by thermal convection, again under the Boussinesq approximation, and in the third by a boundary forcing. The benchmarks 1 and 2 of Marti *et al.* (2013) differ from those of B1 in their use of stress-free boundary conditions, rather than non-slip conditions. In the present work, we remain with the same no-slip boundaries of B1. The use of stress-free boundaries can sometimes cause problems with angular momentum conservation (see the discussion in Jones *et al.* 2011).

The present activity is one of several brethren that have recently been provided to the community. A new benchmark for anelastic convection has recently been described by Jones *et al.* (2011), and solar mean field benchmark has also recently been provided by Jouve *et al.* (2008).

The layout of the paper is as follows. In Section 2, we describe the physical problems to be addressed. In Section 3, we give a brief overview of the different numerical methods that have been employed by the different contributing teams. In Section 4, we present and discuss the results from the different codes.

2 THE NUMERICAL BENCHMARK

Here we define the benchmark in the form of a convection-driven magnetohydrodynamic dynamo in a rotating spherical shell with 'pseudo-vacuum' magnetic boundary condition. We consider a Newtonian fluid with homogeneous and constant material properties, and describe a solution, first studied by Harder & Hansen (2005), that is steadily drifting in azimuth in the rotating frame. Results of the different contributing groups are presented in Section 4.

2.1 Magnetohydrodynamic equations

We employ a geometry of a spherical shell of outer radius r_o and inner radius r_i and fix the radius ratio $r_i/r_o = 0.35$; we denote fluid velocity by $\boldsymbol{u}$, magnetic field by $\boldsymbol{B}$ and temperature by T, and we adopt the Boussinesq approximation. The spherical coordinates will be denoted (r, θ, ϕ) and z is the axis of rotation of the system. The following symbols denote the parameters of the system: $\boldsymbol{\Omega} = \Omega\hat{\boldsymbol{z}}$ is the rotation rate, μ_0 is the permeability of free space, ρ_0 is the density, ΔT is the temperature difference between the fixed temperatures on the inner and outer boundaries, ν, κ and η are the kinematic viscosity, thermal diffusivity and magnetic diffusivity respectively, and α is the thermal expansivity. Gravity is assumed to vary linearly with radius and has value g on the outer boundary. Choosing a non-dimensionalisation for time of $t = (d^2/\eta)t'$, for length of $r = \mathrm{d}r'$ (where $d = r_o - r_i$ is the depth of the shell), for magnetic field of $B = (2\Omega\rho_0\mu_0\eta)^{\frac{1}{2}} B'$ and for temperature of $T = (\Delta T)T'$ (where the primed quantities are the non-dimensional versions), and dropping the primes, we obtain the following equations:

$$\begin{aligned}
\left(Ro\,\frac{\partial}{\partial t} - E\nabla^2\right)\boldsymbol{u} &= Ro\,\boldsymbol{u}\wedge(\nabla\wedge\boldsymbol{u}) + (\nabla\wedge\boldsymbol{B})\wedge\boldsymbol{B} + q\,Ra\,T\,\boldsymbol{r} - \hat{\boldsymbol{z}}\wedge\boldsymbol{u} - \nabla\hat{P},\\
\left(\frac{\partial}{\partial t} - \nabla^2\right)\boldsymbol{B} &= \nabla\wedge(\boldsymbol{u}\wedge\boldsymbol{B}),\\
\left(\frac{\partial}{\partial t} - q\nabla^2\right)T &= -\boldsymbol{u}\cdot\nabla T,
\end{aligned} \tag{1}$$

$$\nabla\cdot\boldsymbol{B} = 0, \quad \nabla\cdot\boldsymbol{u} = 0. \tag{2}$$

These equations have been written in terms of the following dimensionless parameters

$$\begin{aligned}
\text{Magnetic Rossby number } Ro &= \eta/(2\Omega d^2),\\
\text{Ekman number } E &= \nu/(2\Omega d^2),\\
\text{Modified Rayleigh number } Ra &= \frac{g\,\alpha\,\Delta T\,d}{2\Omega\kappa},\\
\text{Roberts number } q &= \kappa/\eta.
\end{aligned} \tag{3}$$

We note that the Magnetic Rossby number is sometimes referred to as the Magnetic Ekman number.

In B1 the timescale chosen was the viscous diffusion timescale, and some readers may find it beneficial to have a conversion between the control parameter definitions used here and those used by B1; these, along with derived quantities, are given in Table 1.

The boundary conditions on T are fixed temperature, thus $T = 1$ at $r = r_i = 7/13$ and $T = 0$ at $r = r_o = 20/13$; boundary conditions on velocity are non-penetration and no slip, thus $\boldsymbol{u} = 0$ on both boundaries. For the magnetic field we implement the condition that the field must be purely radial on both boundaries, a condition that has been used for many years. This condition is significantly easier to implement in all types of discretized versions of (1), since it represents a local condition. Compared to the usual electrically insulating boundary condition that is used in, for example, Christensen *et al.* (2001), it can be easily implemented by requiring that

$$B_\theta = B_\phi = 0 \quad \text{at } r = r_i, r_o, \tag{4}$$

The original integrations of Kageyama *et al.* (1995) as well as subsequent simulations of, for example, Miyagoshi *et al.* (2010) have championed the use of this boundary condition. However, as we see, it can lead to significant differences in the solution, compared to the use of the more conventional insulating boundary condition. The influence of boundary conditions in a Cartesian geometry has been studied by Thelen & Cattaneo (2000) and by Gissinger *et al.* (2008) in a cylindrical geometry in the context of the VKS experiment.

Our benchmark uses exactly the same parameters (Table 2) as used in the original dynamo benchmark (Christensen *et al.* 2001) but with the modified magnetic boundary conditions studied by Harder & Hansen (2005).

Table 1. Conversion table between the present benchmark and B1. The symbols P, P_m and ϵ are the Prandtl number, magnetic Prandtl number and the radius ratio, respectively of B1.

Christensen *et al.* (2001) [B1]	Present benchmark
$E/2$	E
$(1-\epsilon)PRa/2$	Ra
P_m/P	q
$E/(2P_m)$	Ro
$P_m^2 E_{kin}$	E_{kin}
$P_m^2 E_{mag}$	E_{mag}
$P_m\mathbf{u}$	$\mathbf{u}$
$\mathbf{B}/\sqrt{2}$	$\mathbf{B}$
T	T
t/P_m	t

Table 2. Parameters defining the benchmark solution.

E	Ra	q	Ro
5×10^{-4}	32.50	5	10^{-4}

2.2 Initial conditions

The initial conditions for velocity is a quiescent state $\boldsymbol{u} = 0$ and for temperature we adopt the same profile as in Christensen *et al.* (2001)

$$T = \frac{r_\mathrm{o} r_\mathrm{i}}{r} - r_\mathrm{i} + \frac{21}{\sqrt{17920\pi}}(1 - 3x^2 + 3x^4 - x^6)\sin^4\theta\cos 4\varphi, \tag{5}$$

where $x = 2r - r_\mathrm{i} - r_\mathrm{o}$. This describes a conductive state with a perturbation of harmonic degree and order four superimposed. The importance of the initial temperature is in the fourfold symmetry which it brings into the solution.

The initial condition for the magnetic field is very important, as the dynamo for the specified parameters is subcritical, in other words it cannot grow from an arbitrary infinitesimal perturbation; Although a variety of initial conditions has been investigated, it cannot be excluded that different initial conditions may lead to other dynamo solutions. Thus we prescribe the following initial condition for $\boldsymbol{B}$ in real space:

$$\begin{aligned}
B_r &= \frac{1}{\sqrt{2}}\frac{5}{8}\frac{-48\, r_\mathrm{i} r_\mathrm{o} + [4 r_\mathrm{o} + r_\mathrm{i}(4 + 3 r_\mathrm{o})]\, 6r - 4[4 + 3(r_\mathrm{i} + r_\mathrm{o})]\, r^2 + 9 r^3}{r}\cos\theta, \\
B_\theta &= -\frac{1}{\sqrt{2}}\frac{15}{4}\frac{(r - r_\mathrm{i})(r - r_\mathrm{o})(3r - 4)}{r}\sin\theta, \\
B_\phi &= \frac{1}{\sqrt{2}}\frac{15}{8}\sin\pi(r - r_\mathrm{i})\sin 2\theta.
\end{aligned} \tag{6}$$

It is easy to see that $B_\theta = B_\phi = 0$ at r_i and r_o, the condition $\frac{\partial}{\partial r}(r^2 B_r) = 0|_{r_\mathrm{i}, r_\mathrm{o}}$ is satisfied as well.

The magnetic vector $\boldsymbol{B}$ can be written in terms of the toroidal and poloidal scalar fields, T and P:

$$\boldsymbol{B} = \boldsymbol{\nabla} \wedge (T\boldsymbol{r}) + \boldsymbol{\nabla} \wedge \boldsymbol{\nabla} \wedge (P\boldsymbol{r}). \tag{7}$$

The toroidal and poloidal scalars can be decomposed in fully normalized spherical harmonics Y_l^m and radial functions of the form:

$$T = \sum T_l^m(r) Y_l^m(\theta, \phi) \tag{8}$$

with a similar expression for P; here we make use of

$$Y_l^m(\theta, \phi) = P_l^m(\cos\theta)\mathrm{e}^{\mathrm{i}m\phi} \tag{9}$$

where P_l^m is a Legendre function.

Making use of these expansions, the spectral form of the initial magnetic field is

$$\begin{cases}
T_2^0 = \dfrac{1}{\sqrt{2}}\dfrac{5}{4}\sin\pi(r - r_\mathrm{i}), \\
P_1^0 = \dfrac{1}{\sqrt{2}}\dfrac{5}{16}\{-48\, r_\mathrm{i} r_\mathrm{o} + [4 r_\mathrm{o} + r_\mathrm{i}(4 + 3 r_\mathrm{o})]\, 6r - 4[4 + 3(r_\mathrm{i} + r_\mathrm{o})]\, r^2 + 9 r^3\}.
\end{cases} \tag{10}$$

In terms of the magnetic vector potential **A**, we have the initial condition as

$$\begin{cases}
A_r = \dfrac{1}{\sqrt{2}}\dfrac{15}{16} r \sin[\pi(r - r_\mathrm{i})]\cos(2\theta) + f_1(r) + \displaystyle\int \left\{ f_2(r, \theta) + r\frac{\partial f_2(r, \theta)}{\partial r} \right\} \mathrm{d}\theta \\
A_\theta = f_2(r, \theta) \\
A_\phi = \dfrac{1}{\sqrt{2}}\dfrac{5}{16}\{-48 r_\mathrm{i} r_\mathrm{o} + [4 r_\mathrm{o} + r_\mathrm{i}(4 + 3 r_\mathrm{o})]6r - 4[4 + 3(r_\mathrm{i} + r_\mathrm{o})]r^2 + 9r^3\}\sin\theta + K/(r\sin\theta),
\end{cases} \tag{11}$$

where $\boldsymbol{B} = \boldsymbol{\nabla} \wedge \boldsymbol{A}$; f_1, f_2 are arbitrary functions and K is an arbitrary constant. For the calculations performed by Cébron, these functions and constant were taken to be zero.

2.3 The form of the solution

In this section, we describe a steadily drifting solution (where the magnetic and kinetic energies are constant in time) that acts as a dynamo and which is therefore suitable for a benchmark study. The parameters are those suggested by Harder & Hansen (2005) in which a solution exists that has fourfold symmetry in longitude and is symmetric about the equator. Just as in Christensen *et al.* (2001), the solution is steadily drifting and can be expressed in the form $(\boldsymbol{u}, \boldsymbol{B}, T) = f(r, \theta, \varphi - \omega t)$. The influence of the changed boundary conditions is substantial in this

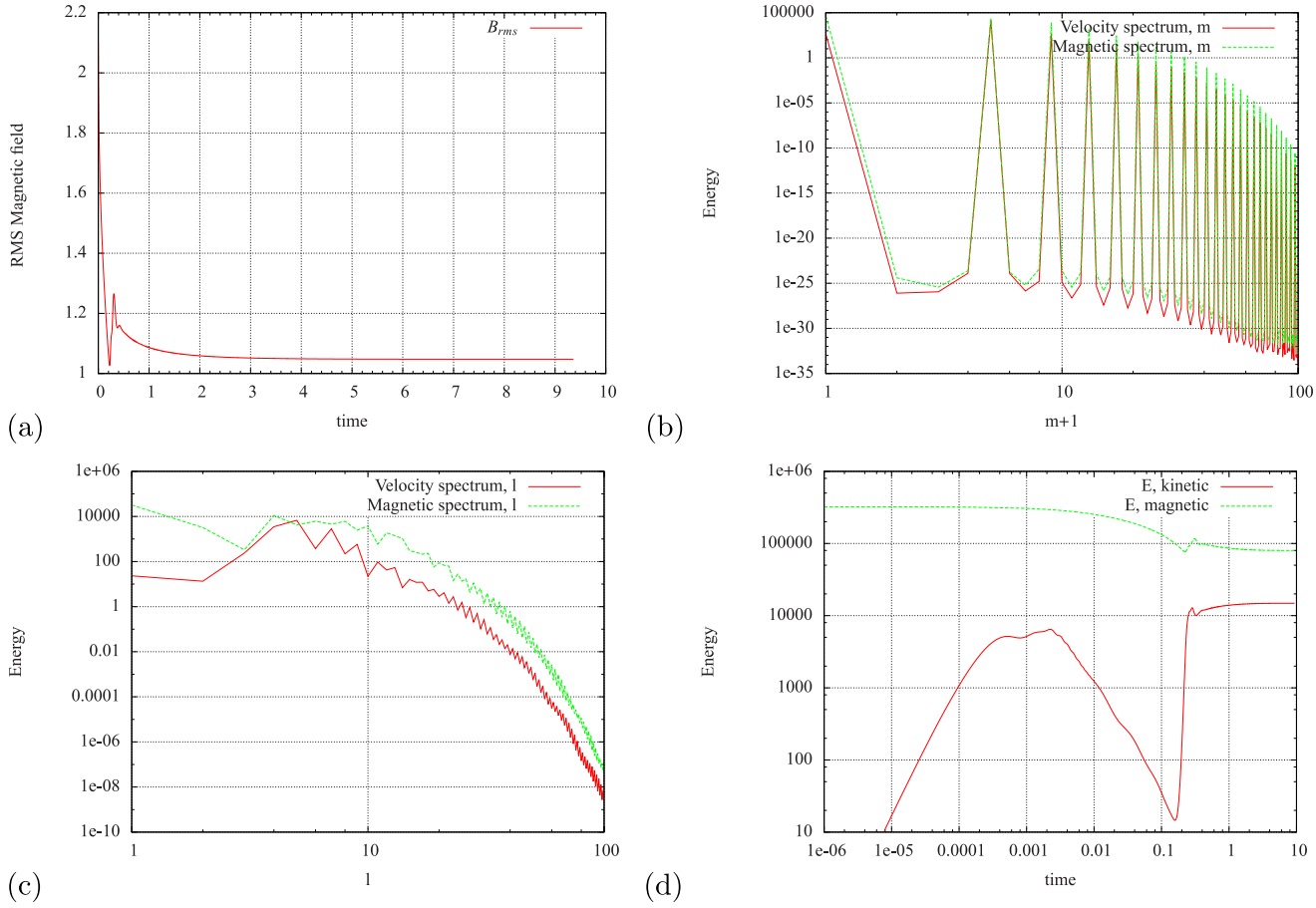

Figure 1. Properties of the solution, computed using a spectral method by SMJ. (a) The evolution of the rms magnetic field versus time, starting from the prescribed initial condition. Although the solution evolves to a pseudo-steady state in a few tenths of a diffusion time, several magnetic diffusion times are required to find a true steady state. (b) The energy spectrum decomposed into azimuthal modes, showing the true fourfold symmetry. (c) The energy spectrum decomposed as a function of spherical harmonic degree, showing twelve orders of magnitude of decrease by spherical harmonic degree 100. (d) The magnetic and kinetic energies on a logarithmic energy and timescale.

regime, because the drift of the solution is completely changed. In case 1 of Christensen *et al.* (2001), the drift rate ω is negative, indicating retrograde drift; in this benchmark the sign of the drift is changed, indicating prograde drift. Figs 1(a) and (d) show the evolution of the field with time, starting with the recommended initial conditions. When the solution is computed with a spherical harmonic-based code, the spectrum can be seen to have fallen off substantially by spherical harmonic degree 100 (Fig. 1 c). By dint of the fourfold symmetry (Fig. 1 b), spherical harmonic-based codes can accurately compute the solution by imposing this symmetry if required; this was implemented by some of the participants. Figs 2–4 show the field and flow structure. Because of the changed boundary condition, we emphasis that, apart from the fourfold symmetry, this solution is not the same as that of B1. The change in the drift rate indicates that the pseudo-vacuum boundary condition cannot be considered to be an approximation to an insulating boundary condition: the physics is entirely altered.

2.4 Requested results

Global averages and local data at specific points were requested from the participating groups. The angular drift speed ω, and magnetic and kinetic energies were requested; the latter two are defined as

$$E_{\rm mag} = \frac{1}{2\,Ro}\int |\mathbf{B}|^2\,{\rm d}V \tag{12}$$

$$E_{\rm kin} = \frac{1}{2}\int |\mathbf{u}|^2\,{\rm d}V. \tag{13}$$

where the integration volume is the fluid shell. Following Christensen *et al.* (2001), we also request local data. A point where local data are to be taken is fixed in the drifting reference frame. We take a point at a mid depth ($r = (r_{\rm i} + r_{\rm o})/2$) in the equatorial plane ($\theta = \pi/2$) whose ϕ-coordinate is given by the conditions $u_r = 0$ and $\frac{\partial u_r}{\partial \varphi} > 0$. For this point u_ϕ, B_θ and T are requested.

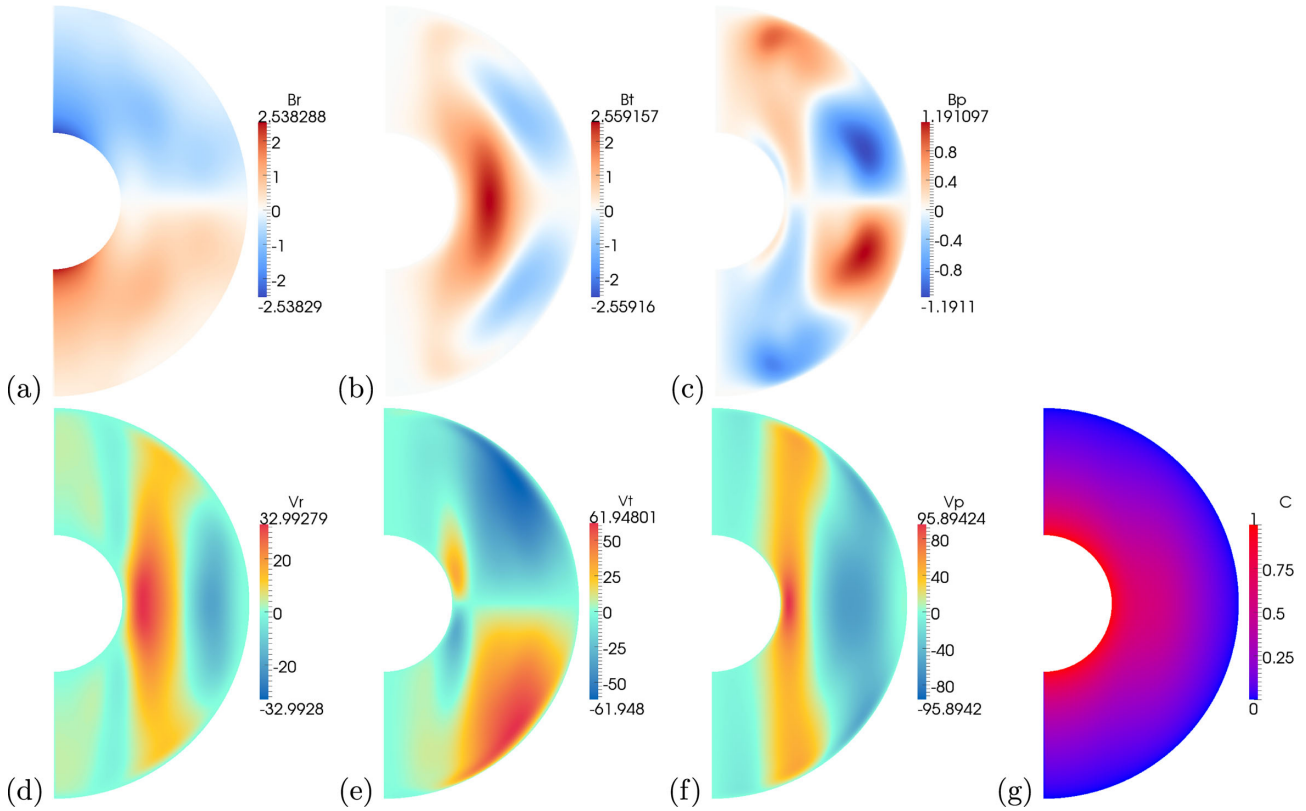

Figure 2. Meridional sections through the solution in the steady state. The plane of the figures is that containing the benchmark point (defined in seq. 2.4). (a) Radial magnetic field. (b) B_θ. (c) B_ϕ. (d) Radial velocity field. (e) v_θ. (f) v_ϕ. (g) Temperature field.

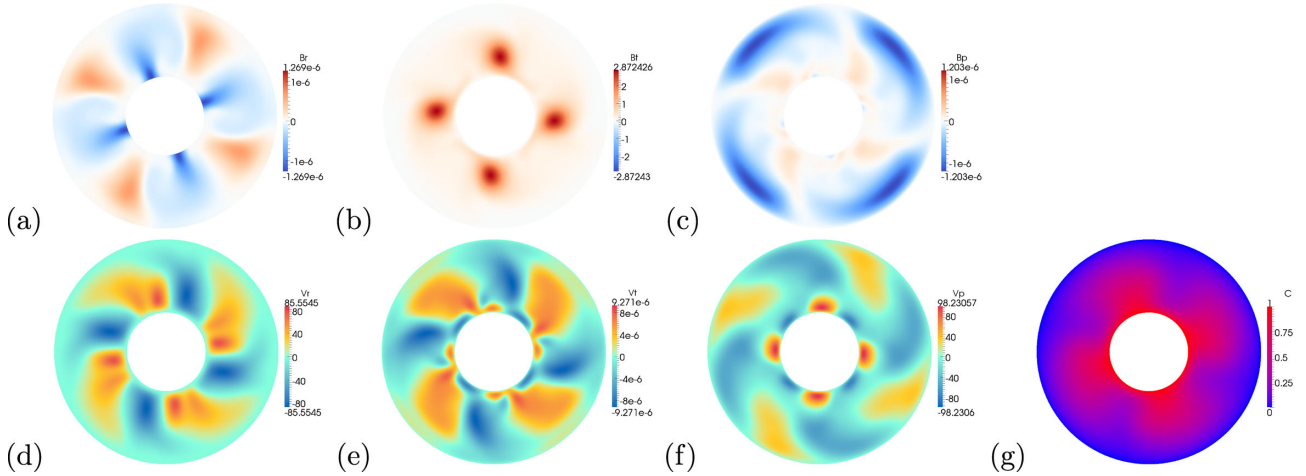

Figure 3. Equatorial sections through the solution in the steady state. (a) Radial magnetic field. (b) B_θ. (c) B_ϕ. (d) Radial velocity field. (e) v_θ. (f) v_ϕ. (g) Temperature field.

3 CONTRIBUTING NUMERICAL CODES

Here we give a short description of the numerical techniques and algorithms used by each simulation group.

Tilgner (T): Pseudospectral code using a spherical harmonic expansion in the angular variables and Chebyshev polynomials in radius, embedded in a poloidal–toroidal representation for magnetic field and velocity. Time stepping is implemented by a combination of an implicit Crank–Nicolson scheme for the diffusion terms and an explicit Adams–Bashforth scheme for the Coriolis and the non-linear terms; both schemes are second order accurate. Early versions of the code are described in Tilgner & Busse (1997) and Tilgner (1999).

Sheyko, Marti & Jackson (SMJ): Spectral simulation using spherical harmonics for the angular component and finite differences in radius. The incompressibility condition is guaranteed by the use of a toroidal–poloidal decomposition of the vector fields. A second order predictor–corrector scheme is used for the time integration. The code was developed by Ashley Willis (see Willis *et al.* 2007), with subsequent optimization for the Cray XMP.

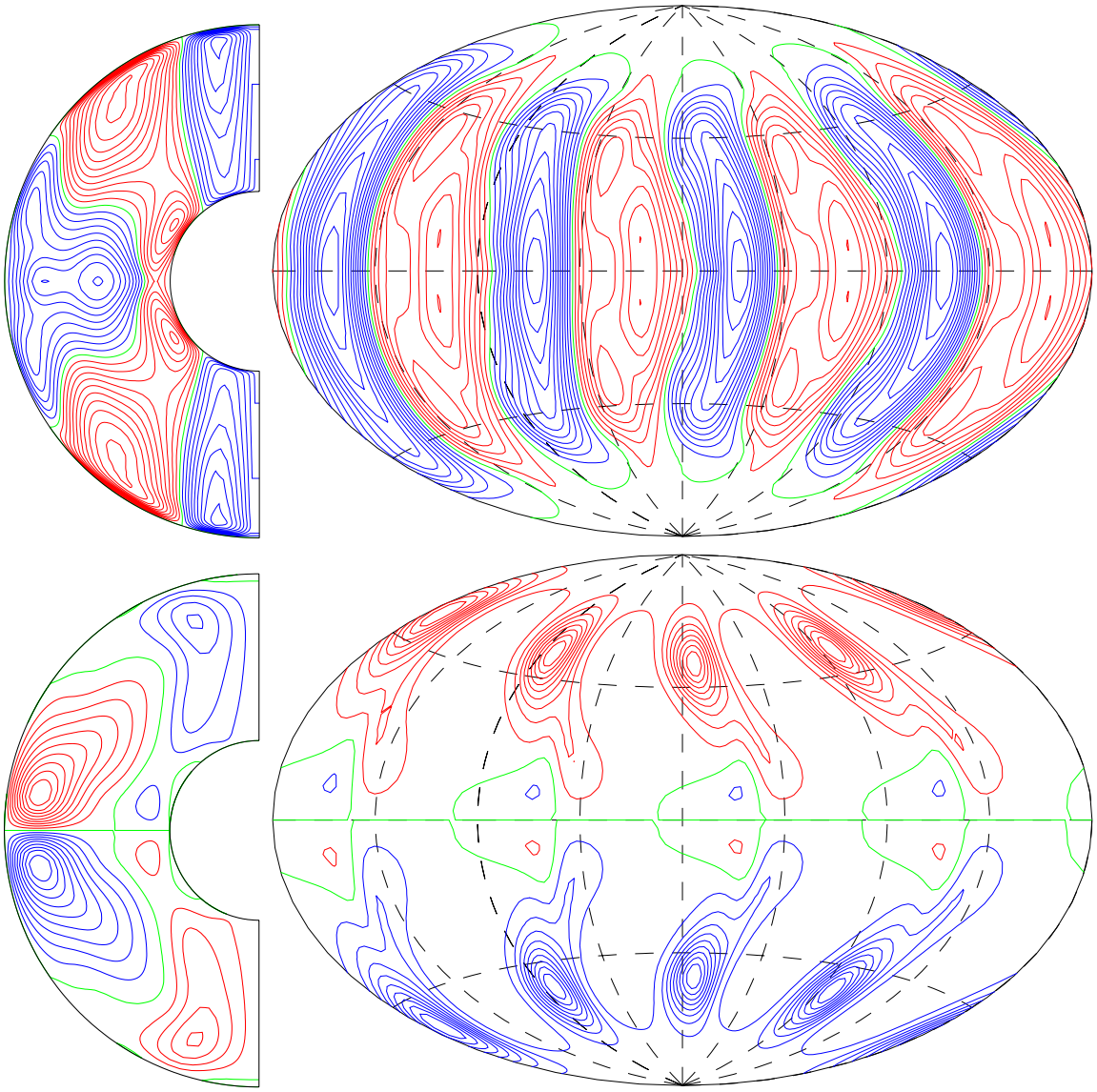

Figure 4. The left-hand column shows isolines of the azimuthally averaged u_φ (top) and B_φ (bottom) in the meridional plane. The right column shows isolines of u_r (top) at mid-radius $r = (r_\mathrm{i} + r_\mathrm{o})/2$ and of B_r (bottom) at the surface of the shell $r = r_\mathrm{o}$.

Takehiro, Sasaki and Hayashi (TSH): Spectral simulation using spherical harmonics for the angular components and Chebychev polynomials in radius (see Sasaki *et al.* 2012). The incompressibility condition is guaranteed by the use of a toroidal–poloidal decomposition of the vector fields. The time integration is performed with a Crank–Nicolson scheme for the diffusive terms and a second order Adams–Bashforth scheme for the other terms.

Simitev and Busse (SB): Pseudospectral numerical code using spherical harmonics expansion in the angular variables and Chebyshev polynomials in radius. Time stepping is implemented by a combination of an implicit Crank–Nicolson scheme for the diffusion terms and an explicit Adams–Bashforth scheme for the Coriolis and the non-linear terms; both schemes are second order accurate. Early versions of the code are described in Tilgner & Busse (1997) and Tilgner (1999) and the code has been extensively modified and used for a number of years Simitev & Busse (2005, 2009, 2012) and Busse & Simitev (2006, 2008).

Cébron (C): Finite element method simulation using the standard Lagrange element P1–P2, which is linear for the pressure field and quadratic for the velocity field, and a Galerkin Least-Squares (GLS) stabilization method (Hauke & Hughes 1994). Quadratic Lagrange elements are used for the temperature field, and quadratic Nédélec (edge) elements are used for vector potential $\mathbf{A}$, such that $\mathbf{B} = \nabla \wedge \mathbf{A}$. The (unstructured) mesh is made of prisms in the boundary layer and tetrahedrons in the bulk. The incompressibility of the velocity field is imposed using a penalty method. The time stepping uses the implicit differential-algebraic solver (IDA solver), based on variable-coefficient backward differencing formulas (e.g. Hindmarsh *et al.* 2005). The integration method in IDA is variable-order, the order ranging between 1 and 5. At each time step, the system is solved in a fully coupled way with a geometric multigrid GMRES iterative solver. This is all implemented via the commercial code COMSOL Multiphysics® (see Cébron *et al.* 2012, for further details).

Ribeiro, Nore, and Guermond (RNG): Hybrid Fourier and finite element method using a Fourier decomposition in the azimuthal direction and the standard Lagrange elements P1–P2 in the meridian section (with P1 for the pressure and P2 for the velocity field). The meridian mesh is made of quadratic triangles. The velocity and pressure are decoupled by using the rotational pressure-correction method. The timestepping uses the second-order Backward Difference Formula (BDF2). The non-linear terms are made explicit and approximated using second-order extrapolation in time. The code is parallelized in Fourier space and in meridian sections (domain decomposition with METIS Karypis & Kumar 2009) using MPI and PETSC (Portable, Extensible Toolkit for Scientific Computation) Balay *et al.* (1997, 2012a,b). This is implemented in the code SFEMaNS (for Spectral/Finite Element method for Maxwell and Navier–Stokes equations) Guermond *et al.* (2007, 2009, 2011).

Vantieghem (V): Massively MPI-parallel unstructured finite-volume code (Vantieghem 2011), based on a domain decomposition with METIS (Karypis & Kumar 2009). For this benchmark, a grid of the cubed-sphere type was used. All the spatial discretization operators are based on finite-difference-like stencils. To advance the equations in time, a semi-implicit Crank–Nicolson/Adams–Bashforth formulation is used for the non-linear terms, and a Crank–Nicolson discretization for the diffusive, Coriolis and buoyancy terms. The pressure–velocity splitting is based on a canonical fractional step-method (Kim & Moin 1985). A Lagrange multiplier (termed magnetic pressure) is added to the induction equations to enforce the divergence-free constraint on $\mathbf{B}$. The pressure Poisson equations are solved using a BiCGstab(2)-method.

Zhan and Schubert (ZS): This approach uses the 'element-by-element' finite element method described in Chan *et al.* (2007). The magnetic field itself is used as the field that is solved for (without the use of a vector potential) and the divergence-free condition is implemented using a Lagrange multiplier. Quadratic Hood-Taylor elements are used for $\mathbf{u}$, T and $\mathbf{B}$ and linear elements for the pressure.

4 RESULTS

Fig. 5 summarizes the results from the contributing codes. We plot them as a function of resolution R based on the number of degrees of freedom in the calculation. For grid-based codes, R is simply $N_{\rm grid}^{1/3}$ where $N_{\rm grid}$ is the number of elements or volumes in the calculation. For spectral codes $R = [N_r \cdot (L_{\max}(2M_{\max}+1) - M_{\max}^2 + M_{\max} + 1)]^{1/3}$. The same approach was used in B1.

It is clear that all participants succeeded in finding the correct solution to the benchmark. The only variability is in the fidelity with which the solution is determined, but in all cases the agreement is better than 6 per cent, this worst case being for the medium-resolution calculation of C; we neglect the two extremely low resolution results supplied by T in this respect. The benchmark by nature is a very smooth and regular solution, and therefore spectral methods have a distinct advantage. It is clear that accurate solutions can be computed with a truncation level of degree 42 in spherical harmonics and either 33 Chebychev polynomials in radius or about 80 finite difference points in radius. Fig. 5 shows that the spectral methods of SMJ, T, TSH and SB all agree almost perfectly with one another and can be used to create a reference solution. It is unfortunate that two of the local codes only present one point. In the case of C, using the commercial code COMSOL, this is because the version of the code used is purely serial; it therefore takes a tremendously long time (several months on a single core) to run the 5.12 diffusion times of the solution reported. The two local codes that allow us a comparison of rates of convergence are the finite volume code by V and the finite element code by ZS. The ZS code appears to have reached converged values for all quantities. For the local values these are very accurate, with discrepancy from spectral solutions at the level of 0.21–0.52 per cent; for an unknown reason the discrepancy is larger when global quantities are compared, with the discrepancy being at the level of 1.4 per cent in the magnetic energy. The finite volume code by V needs higher resolution for convergence to have been demonstrated. Drifting solution can be a problem for local codes because the solution drift with respect to the grid leads to additional oscillations even in the energies. To illustrate the size of the problem, for solution V the reported values are averages over 0.5 magnetic diffusion times. Typical amplitudes for the oscillation of the magnetic energy are 0.3 per cent (at resolution 64), 0.12 per cent (96) and 0.06 per cent (128); note that these values are small compared to the difference with the pseudospectral solution, so that the averaging interval does not fundamentally affect the reported values.

Definitive values for the benchmark are taken from the most highly resolved calculations of SMJ, T, TSH and SB (see Tables 3 and 4), though note a very small discrepancy in the drift rate computed by TSH; this quantity is usually the most difficult to determine precisely, as in the sister exercises B1 and Marti *et al.* (2013). We present definitive values for the benchmark with error corridors in Table 5.

Indicative time steps used by the codes at the highest resolutions are 4×10^{-6} (V), 3×10^{-6} (SB), 2.5×10^{-6} (TSH) and 1.6×10^{-5} (SMJ). Code V was run on 512 processors at the highest resolution. Note that the choice of magnetic Prandtl number 5 results in a dynamo solution that is close to the onset of stable dynamo action. Therefore, the stable solution only settles in slowly, as can be observed from Fig. 1(a), and long time integrations are required to obtain stable solutions. This aspect made this benchmark particularly challenging, especially for local codes that are computationally much more expensive than spectral ones.

5 DISCUSSION

As was the case for the benchmark B1 and the sister study of Marti *et al.* (2013), dynamos in the weakly driven regime have a simple structure that offer a distinct advantage to spectral methods. Despite the view that spectral codes will be replaced by local methods because of superior parallelism, it is clear that spectral codes will continue to have an important role on strictly spherical problems. The current code of SMJ (originating with Willis *et al.* 2007) shows good scaling on up to 1200 processors on a CRAY XE6 architecture, while the fully spectral code of Marti (described in Marti *et al.* 2013) has been tested on up to 2000 processors, again with good performance.

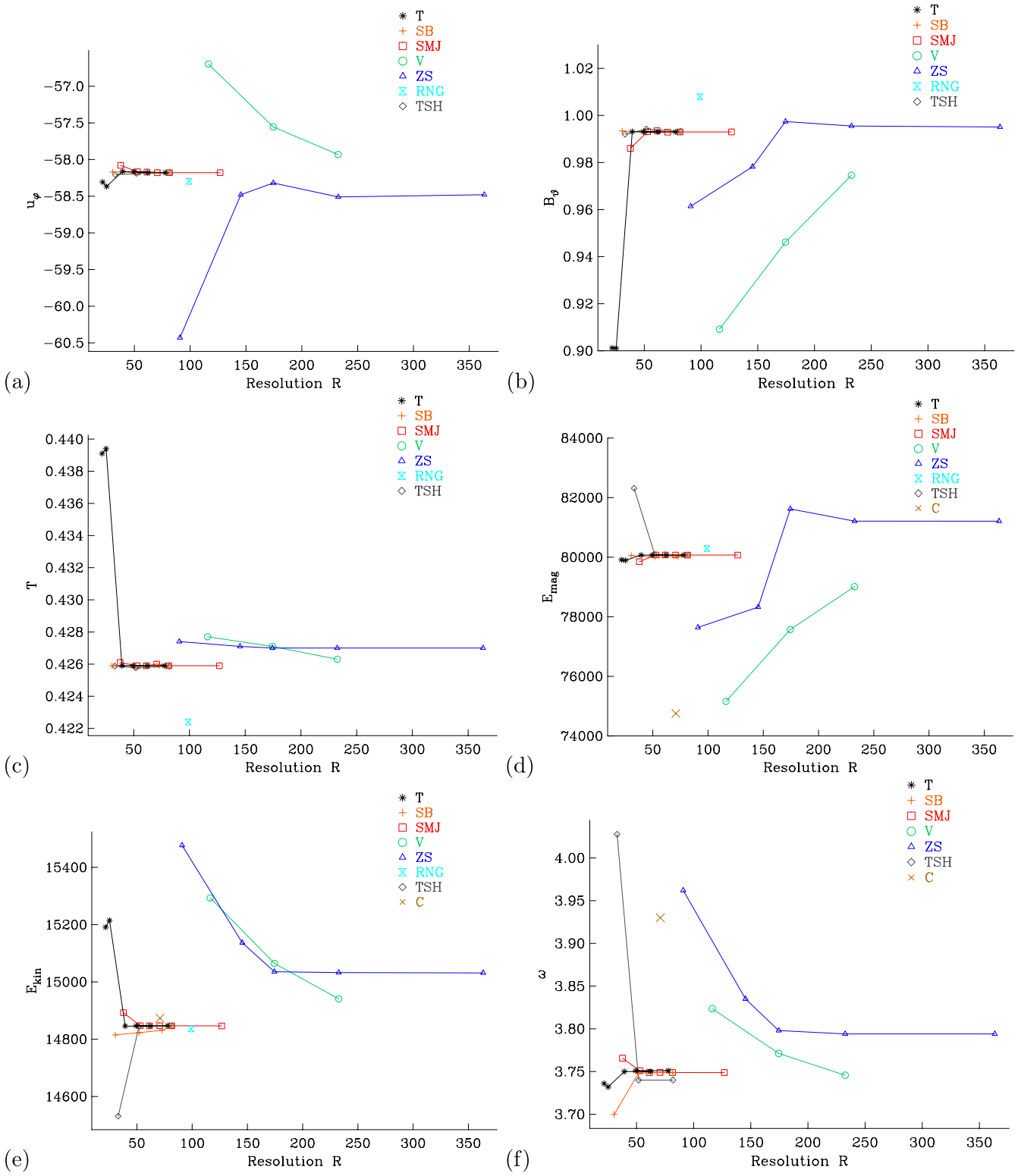

Figure 5. Results of the different codes. (a) u_ϕ at the requested point in the equatorial plane ($\theta = \pi/2$) whose r and ϕ-coordinates are given in Section 3. For the key to the codes used, see Section 4. (b) B_θ at the same point. (c) Temperature T at the same point. (d) Magnetic energy $E_{\rm mag}$ defined by (13). (e) Kinetic energy $E_{\rm kin}$ defined by (13). (f) The drift rate ω. No values were contributed by Cébron to (a), (b) or (c), and no value was given by RNG for (f). For contributor ZS the resolution has been taken to be $6^{1/3}$ times the number of radial nodes, in agreement with Chan *et al.* (2007).

Table 3. Spectral codes contributing to the benchmark. The number of significant figures given are those reported by the authors, thus there are different numbers of significant figures, particularly for local quantities. N_r, L and M are the number of radial nodes or modes, and maximum spherical harmonic degree and order, respectively. R is the overall resolution in one direction. The code by RNG is a mixed spectral-finite element.

N_r	L	M	R	u_ϕ	B_θ	T	$E_{\rm mag}$	$E_{\rm kin}$	ω	Author
50	32	29	37	−58.0792	0.986	0.4261	79849.4	14892.8	3.7656	SMJ
80	42	42	52	−58.167	0.9931	0.4259	80076.3	14847.3	3.751	SMJ
96	48	48	61	−58.1705	0.9935	0.4259	80076.2	14846.9	3.7489	SMJ
96	60	53	70	−58.1796	0.9929	0.426	80074.7	14847.2	3.749	SMJ
128	64	64	81	−58.1786	0.993	0.4259	80072.7	14846.9	3.7489	SMJ
200	100	100	126	−58.1786	0.993	0.4259	80072.7	14846.5	3.7488	SMJ
33	32	64	33	−58.2075	0.99201	0.42587	82313.8	14531.4	4.02768	TSH
33	64	128	51	−58.1901	0.99423	0.42577	80082.1	14844.1	3.73999	TSH
33	128	256	81	−58.1825	0.99318	0.42587	80073.1	14845.7	3.73999	TSH
21	21	21	21	−58.307	0.9012	0.4391	79914.4	15191.1	3.736	T
33	21	21	25	−58.367	0.9011	0.4394	79893.9	15214.9	3.732	T
33	42	42	39	−58.1615	0.9931	0.4259	80071.2	14845.8	3.75	T
33	84	84	62	−58.1785	0.993	0.4259	80072.7	14846	3.75	T
65	42	42	49	−58.165	0.993	0.4259	80067.8	14846.8	3.751	T
65	84	84	77	−58.179	0.993	0.4259	80068.3	14847.2	3.751	T
33	42	11	30	−58.1695	0.9934	0.4259	80057.2	14815.3	3.6998	SB[a]
33	64	65	51	−58.1765	0.9928	0.4259	80000.7	14822.8	3.7484	SB
41	96	97	72	−58.1775	0.9929	0.4259	80025.7	14831.3	3.7488	SB
129	64	65	81	−58.177	0.9929	0.4259	80068.9	14845.2	3.7487	SB
90	180	60	99	−58.2985	1.0079	0.4224	80292.2	14836		RNG[a, b]

[a]This was run with assumed fourfold symmetry.
[b]The three resolutions (90, 180, 60) refer to N_r, N_z and N_ϕ, respectively.

Table 4. Local codes contributing to the benchmark. For V and ZS, $R = 6^{1/3}N$ is a measure of the overall resolution, since N is the radial resolution. In the case of V this is exact, since a cubed sphere with $6N^3$ gridpoints is used; for ZS the relationship is approximate but quite accurate.

N	R	u_ϕ	B_θ	T	$E_{\rm mag}$	$E_{\rm kin}$	ω	Author
64	116	−56.697	0.9092	0.4277	75162.4	15293.7	3.8236	V
96	174	−57.555	0.9462	0.4271	77572.0	15064.7	3.7712	V
128	232	−57.932	0.9746	0.4263	79012.3	14940.9	3.7457	V
50	91	−60.43	0.9614	0.4274	77643.3	15476.8	3.962	ZS
80	145	−58.48	0.9782	0.4271	78324.1	15136.6	3.835	ZS
96	174	−58.32	0.9974	0.4270	81621.7	15035.7	3.798	ZS
128	232	−58.51	0.9955	0.4270	81211.4	15032.7	3.794	ZS
200	363	−58.48	0.9951	0.4270	81209.6	15031.5	3.794	ZS
	71				74756.4	14873.4	3.93	C

We should perhaps comment on the overall accuracy of local codes on these spherical problems. In the original B1 dynamo benchmark, the code of Chan *et al.* (2007) showed agreement with case 1 at a level of 7.7 per cent, a discrepancy that must largely be attributable to the difficulties in handling an insulating exterior. The present benchmark dispenses with that difficulty, and the better agreement at the level of 1.4 per cent reported by ZS must now be attributable to the actual solution of the differential equations themselves in the fluid. We note parenthetically that the finite volume formulation of Harder & Hansen (2005) shows a similar level of discrepancy in the case 1 benchmark of B1, at a level of about 6 per cent (reported in Wicht *et al.* 2009). For the case 1 benchmark, the finite element formulation of Matsui & Okuda (2005) has achieved agreement at a level of 3.6 per cent, while the so-called 'control volume' method of Simkanin & Hejda (2009) achieves an agreement with the case 2 benchmark of B1 of better than 6 per cent in all variables; it is again the drift rates that are the most difficult to retrieve accurately.

The advantage of local methods is in their flexibility to work in non-spherical geometries. The code of RNG has been used extensively in a cylindrical geometry to study the Von Karman dynamo (Guermond *et al.* 2009, 2011); and the code of Chan *et al.* (2007) used by ZS has been used to simulate the fluid dynamics in rotating spheroids (see Zhang *et al.* 2012, and references to other applications therein). Indeed,

Table 5. Recommended values for the benchmark, derived from the four spectral solutions, along with suggested error corridors expressed in absolute and percentage terms. For the estimate of ω we omitted the TSH solution.

	u_ϕ	B_θ	T	$E_{\rm mag}$	$E_{\rm kin}$	ω
Value	−58.179	0.9930	0.42589	80071	14846	3.7495
Error	0.002	0.0001	0.00001	2.5	1	0.001
Percentage error	0.004 per cent	0.01 per cent	0.002 per cent	0.003 per cent	0.006 per cent	0.03 per cent

Wu & Roberts (2009) have used a gridpoint method to simulate a dynamo in a spheroid that is driven by precession, and the finite element method has been used by Cébron *et al.* (2012) to perform MHD simulations in a triaxial ellipsoid. These applications are clearly the *forté* of local methods.

To summarize, as we noted in Section 1, it is particularly gratifying to see that local methods based on both **A** and **B** formulations are able to perform equally well. No account was taken in this exercise of the relative efficiency of the different codes, in terms of the time taken to solution. This will form a focus of future efforts that the community will undertake.

ACKNOWLEDGEMENTS

This work was partly funded by ERC grant 247303 'MFECE' to AJ. AJ and PM acknowledge SNF grant 200021-113466; AJ/PM/AS and SV are grateful for the provision of computational resources by the Swiss National Supercomputing Centre (CSCS) under project IDs s225 and s369, respectively. For this work, DC was supported by the ETH Zurich Postdoctoral fellowship Progam as well as by the Marie Curie Actions for People COFUND Program.

REFERENCES

Balay, S., Gropp, W.D., McInnes, L.C. & Smith, B.F., 1997. Efficient management of parallelism in object-oriented numerical software libraries, in *Modern Software Tools in Scientific Computing,* pp. 163–202, ed. Arge, E., Birkhauser Press.

Balay, S. *et al.*, 2012a. PETSc users manual revision 3.3.

Balay, S. *et al.*, 2012b. PETSc Web page. Available at: http://www.mcs.anl.gov/petsc.

Brackbill, J.U. & Barnes, D.C., 1980. The effect of nonzero B on the numerical solution of the magnetohydrodynamic equations, *J. Comp. Phys.,* **35**(3), 426–430.

Busse, F. & Simitev, R., 2008. Toroidal flux oscillation as possible cause of geomagnetic excursions and reversals, *Phys. Earth planet. Inter.,* **168**(3), 237–243.

Busse, F.H. & Simitev, R.D., 2006. Parameter dependences of convection-driven dynamos in rotating spherical fluid shells, *Geophys. Astrophys. Fluid Dyn.,* **100**(4–5), 341–361.

Cébron, D., Le Bars, M., Maubert, P. & Le Gal, P., 2012. Magnetohydrodynamic simulations of the elliptical instability in triaxial ellipsoids, *Geophys. Astrophys. Fluid Dyn.,* **106**(4–5), 524–546.

Chan, K.H., Zhang, K., Li, L. & Liao, X., 2007. A new generation of convection-driven spherical dynamos using EBE finite element method, *Phys. Earth planet. Inter.,* **163**(1–4), 251–265.

Christensen, U. *et al.*, 2009. Erratum to "A numerical dynamo benchmark" [Phys. Earth Planet. Int. 128 (14) (2001) 25–34], *Phys. Earth planet. Inter.,* **172**(3–4), 356.

Christensen, U.R. *et al.*, 2001. A numerical dynamo benchmark, *Phys. Earth planet. Inter.,* **128,** 25–34.

Gissinger, C., Iskakov, A., Fauve, S. & Dormy, E., 2008. Effect of magnetic boundary conditions on the dynamo threshold of von kármán swirling flows, *Europhys. Lett.,* **82**(2), doi:10.1209/0295-5075/82/29001.

Glatzmaier, G.A. & Roberts, P.H., 1995. A three-dimensional convective dynamo solution with rotating and finitely conducting inner core and mantle, *Phys. Earth planet. Inter.,* **91**(1–3), 63–75.

Guermond, J.-L., Laguerre, R., Léorat, J. & Nore, C., 2007. An interior penalty galerkin method for the mhd equations in heterogeneous domains, *J. Comput. Phys.,* **221**(1), 349–369.

Guermond, J.-L., Laguerre, R., Léorat, J. & Nore, C., 2009. Nonlinear magnetohydrodynamics in axisymmetric heterogeneous domains using a fourier/finite element technique and an interior penalty method, *J. Comput. Phys.,* **228**(8), 2739–2757.

Guermond, J.-L., Léorat, J., Luddens, F., Nore, C. & Ribeiro, A., 2011. Effects of discontinuous magnetic permeability on magnetodynamic problems, *J. Comput. Phys.,* **230**(16), 6299–6319.

Guervilly, C. & Cardin, P., 2010. Numerical simulations of dynamos generated in spherical Couette flows, *Geophys. Astrophys. Fluid Dyn.,* **104**(2–3), 221–248.

Harder, H. & Hansen, U., 2005. A finite-volume solution method for thermal convection and dynamo problems in spherical shells, *Geophys. J. Int.,* **161,** 522–532.

Hauke, G. & Hughes, T., 1994. A unified approach to compressible and incompressible flows, *Comp. Methods appl. Mech. Eng.,* **113**(3–4), 389–395.

Hindmarsh, A.C., Brown, P.N., Grant, K.E., Lee, S.L., Serban, R., Shumaker, D.E. & Woodward, C.S., 2005. Sundials: suite of nonlinear and differential/algebraic equation solvers, *ACM Trans. Math. Softw.,* **31**(3), 363–396.

Jones, C.A., Boronski, P., Brun, A.S., Glatzmaier, G.A., Gastine, T., Miesch, M.S. & Wicht, J., 2011. Anelastic convection-driven dynamo benchmarks, *Icarus,* **216**(1), 120–135.

Jouve, L. *et al.*, 2008. A solar mean field dynamo benchmark, *A&A,* **483**(3), 949–960.

Kageyama, A., Sato, T., Watanabe, K., Horiuchi, R., Hayashi, T., Todo, Todo., Watanabe, Y.H. & Takamaru, H., 1995. Computer simulation of a magnetohydrodynamic dynamo. II, *Phys. Plasmas,* **2**(5), 1421–1431.

Karypis, G. & Kumar, V., 2009. METIS: Unstructured graph partitioning and sparse matrix ordering system, version 4.0. Available at: http://www.cs.umn.edu/metis.

Kim, J. & Moin, P., 1985. Application of a fractional-step method to incompressible Navier-Stokes equations, *J. Comput. Phys.,* **59**(2), 308–323.

Marti, P. *et al.*, 2013. Full sphere hydrodynamic and dynamo benchmarks, *Geophys. J. Int.,* submitted.

Matsui, H. & Okuda, H., 2005. Mhd dynamo simulation using the geofem platform? verification by the dynamo benchmark test, *Int. J. Comput. Fluid Dyn.,* **19**(1), 15–22.

Miyagoshi, T., Kageyama, A. & Sato, T., 2010. Zonal flow formation in the Earth's core, *Nature,* **463**(7282), 793–796.

Roberts, P.H., Glatzmaier, G.A. & Clune, T.L., 2010. Numerical simulation of a spherical dynamo excited by a flow of von kárman type, *Geophys. Astrophys. Fluid Dyn.,* **104**(2–3), 207–220.

Sasaki, Y., Takehiro, S. & Hayashi, Y.-Y. & SPMODEL Development Group., 2012. Project of MHD Dynamo in rotating spheres and spherical shells. Available at: http://www.gfd-dennou.org/library/dynamo/.

Simitev, R. & Busse, F., 2005. Prandtl-number dependence of convection-driven dynamos in rotating spherical fluid shells, *J. Fluid Mech.,* **532,** 365–388.

Simitev, R. & Busse, F., 2012. How far can minimal models explain the solar cycle? *Astrophys. J.,* **749**(1), **9**.

Simitev, R.D. & Busse, F.H., 2009. Bistability and hysteresis of dipolar dynamos generated by turbulent convection in rotating spherical shells, *EPL (Europhys. Lett.),* **85**(1), doi:10.1209/0295-5075/85/19001.

Simkanin, J. & Hejda, P., 2009. Control volume method for hydromagnetic dynamos in rotating spherical shells: Testing the code against the numerical dynamo benchmark, *Stud. Geophys. Geod.,* **53**(1), 99–110.

Thelen, J.-C. & Cattaneo, F., 2000. Dynamo action driven by convection: the influence of magnetic boundary conditions, *Mon. Notices R. Astron. Soc.,* **315**(2), L13–L17.

Tilgner, A., 1999. Spectral methods for the simulation of incompressible flows in spherical shells, *Int. J. Numer. Methods Fluids,* **30**(6), 713–724.

Tilgner, A. & Busse, F., 1997. Finite-amplitude convection in rotating spherical fluid shells, *J. Fluid Mech.,* **332**(1), 359–376.

Tóth, G., 2000. The $\nabla \cdot \mathbf{B} = 0$ constraint in shock-capturing magnetohydrodynamics codes, *J. Comp. Phys.,* **161**(2), 605–652.

Vantieghem, S., 2011. Numerical simulations of quasi-static magnetohydrodynamics using an unstructured finite volume solver: development and applications, *PhD thesis,* Universitée Libre de Bruxelles.

Wicht, J., Stellmach, S. & Harder, H., 2009. Numerical models of the geodynamo: from fundamental cartesian models to 3D simulations of field reversals, in *Geomagnetic Field Variations,* Advances in Geophysical and Environmental Mechanics and Mathematics, pp. 107–158. Springer.

Willis, A.P., Sreenivasan, B. & Gubbins, D., 2007. Thermal core mantle interaction: exploring regimes for locked dynamo action, *Phys. Earth planet. Inter.,* **165**(1–2), 83–92.

Wu, C.-C. & Roberts, P.H., 2009. On a dynamo driven by topographic precession, *Geophys. Astrophys. Fluid Dyn.,* **103**(6), 467–501.

Zhang, K., Chan, K.H. & Liao, X., 2012. Asymptotic theory of resonant flow in a spheroidal cavity driven by latitudinal libration, *J. Fluid Mech.,* **692,** 420–445.